RSC Advances

PAPER

View Article Online
View Journal | View Issue

Cite this: *RSC Adv.*, 2015, **5**, 56232

Fine control over the morphology and photocatalytic activity of 3D ZnO hierarchical nanostructures: capping *vs.* etching†

Jawayria Mujtaba,[a] Hongyu Sun,*[a] Fang Fang,[a] Mashkoor Ahmad[b] and Jing Zhu*[a]

Received 6th May 2015
Accepted 22nd June 2015

DOI: 10.1039/c5ra08325g

www.rsc.org/advances

ZnO 3D hierarchical structures (3DHNs) with different morphologies have been selectively synthesized at room temperature by using potassium hydroxide (KOH) and citric acid (CA) as an etchant and capping agent, respectively. A possible formation mechanism based on capping–etching competitive interactions has been proposed for the formation of distinct ZnO 3DHNs under different growth conditions. The photocatalytic performance for the degradation of organic contaminants can be improved by fine tuning the morphology of the 3DHNs.

1. Introduction

Low-dimensional metal and/or semiconductor nanostructures, *e.g.* nanoparticles, nanowires/nanotubes and nanosheets, have been extensively studied due to their interesting and unique electronic, optical, thermal, mechanical and magnetic properties, and applications in the fields of energy and catalysis.[1–5] Assembling those low-dimensional nanoscale building blocks into three-dimensional (3D) complex micro-/nanoarchitectures has attracted tremendous interest for their intriguing structural features and great potential in a myriad of applications.[6–9] Such 3D hierarchical structures (3DHNs) not only inherit the excellent properties of the single nanobuilding block but also show special properties and multiple functionalities which are induced by the interaction of the low-dimensional structures.[6] On the other hand, facile synthesis of 3DHNs with tunable size, morphology of the constituted nanobuilding blocks and their assemble fashion is crucial, since the functional properties are dictated by these structural parameters.[10–12] In this regard, fine control over the morphology of low-dimensional nanostructures is highly desirable.

"Bottom-up" synthesis with the aid of suitable capping agents has allowed the precise control of nanostructures with well-defined morphology.[1] The addition of a capping agent can change the order of surface energies for different crystallographic facets, and thus has a vital effect on their relative growth rates. The plane with a lower addition rate will be exposed more on the final nanocrystal surface.[1] Yang and co-authors reported unconventional TiO_2 single crystals with curved surfaces, which are composed of quasi continuous high-index microfacets.[13] It is suggested that the chemisorbed organic citric acid and inorganic hydrofluoric acid as synergistic capping agents play key roles in the formation of such novel morphology. By using controlled seeded growth and citrate anions that selectively adsorb on ZnO basal planes as the capping agent, Tian *et al.* prepared various complex and oriented ZnO nanostructures, which has shown enhanced abilities for photocatalytic decompositions of volatile organic compounds.[14] "Top-down" method based on chemical/electrochemical etching has been proved to be another effective approach to control morphology, size, and composition of nanostructures simultaneously.[15–17] By selective dissolving of the vulnerable component from starting materials, this strategy leads to yield nanostructures with fantastic morphology. For example, Chen *et al.* synthesized highly crystalline Pt–Ni nanoframes with 3D electrocatalytic surfaces through etching the initial crystalline $PtNi_3$ polyhedra in solution, which exhibits enhanced electrocatalytic activity.[18] Yang and co-authors demonstrated a novel anisotropic etching route to obtain complex nanoparticle morphology by controlling the kinetics and selectivity of etchant solutions.[19] Our group has first developed metal-catalyzed electroless etching technique for the fabrication of silicon nanowire arrays by using oxidizing HF solution as etchant.[20] We previously reported the facile synthesis of ZnO 3DHNs assembled by different nanobuilding blocks (nanosheet, nanoneedle) through chemical etching method. The morphology of the 3DHNs can be well controlled by simply changing the concentration of the etchant.[21,22]

As a typical direct wide band gap (E_g = 3.37 eV) semiconductor with notable piezoelectric behavior, ZnO has been

[a]*Beijing National Center for Electron Microscopy, School of Materials Science and Engineering, The State Key Laboratory of New Ceramics and Fine Processing, Key Laboratory of Advanced Materials (MOE), Tsinghua University, Beijing 100084, China. E-mail: hysuny@mail.tsinghua.edu.cn; jzhu@mail.tsinghua.edu.cn*

[b]*Nanomaterials Research Group, Physics Division, Pakistan Institute of Nuclear Science and Technology, P.O. Nilore, Islamabad 44000, Pakistan*

† Electronic supplementary information (ESI) available: FESEM images of the ZnO nanostructures with the addition of different amount of CA, degradation of RhB solutions in the presence of different ZnO photocatalysts under visible light irradiation. See DOI: 10.1039/c5ra08325g

extensively studied due to its unique properties and potential applications in room temperature nanolasers, nanogenerators, solar cells and photocatalyst.[23–27] Compared to the mono-morphological low dimensional structures (including nanowires, nanobelts, nanorings, nanohelixs and so on), ZnO with complex 3DHNs, such as dandelion-like, flower-like, and sea-urchin shape, have been demonstrated to show enhanced properties for applications like sensors and photocatalysts.[28–30] Many methods, *e.g.* hydrothermal/solvothermal, electrochemical deposition, and thermal evaporation have been successfully employed to produce ZnO 3DHNs,[14,31–47] and the morphology of the products can be successfully controlled by carefully choosing capping agents or etchants.[14,42–47] However, the morphology of the yielded products is controlled by adding capping agents or etchants alone. Less attention has been paid to study the morphology features with the addition of capping agents and etchants together. Since the capping and etching are two competitive and contrary interactions, it is anticipated that manipulating the "Bottom-up" and "Top-down" processes simultaneously could bring out 3DHNs with novel morphology, as well as give us more ability to fine tune the functionalities.

In this work, we describe a simple wet chemical method to synthesis ZnO 3DHNs at room temperature just by using zinc nitrate hexahydrate and zinc foil as source materials, potassium hydroxide and citric acid as etchant and capping agent, respectively. The morphology of the 3DHNs, including needle-sheet flowers and needle flowers, can be well controlled by changing the concentration of the reactant. On the basis of the capping agent concentration-dependent experimental results, the possible formation mechanism of the ZnO 3DHNs is discussed. The room temperature photoluminescence (PL) properties of the products are also studied. The photocatalytic results indicate that the ZnO NFs sample exhibits an enhanced photocatalytic performance for the degradation of organic contaminants, which may be due to the distinct structural features and high optical quality. It is anticipated that the present findings should be applicable to the synthesis and modification of other materials by careful selecting suitable capping agents and etchants.

2. Experimental

2.1 Materials

Zinc nitrate hexahydrate ($Zn(NO_3)_2 \cdot 6H_2O$), zinc sheet (99.9%), potassium hydroxide (KOH), and citric acid ($C_6H_8O_7$, CA) were purchased from Sinopharm Chemical Regent Co. Ltd. *N*,*N*,*N*′,*N*′-Tetraethylrhodamine B (RhB) was obtained from Beijing Modern Eastern Fine Chemical. Other chemicals were of analytical grade and were used without further purification. All solutions used during the experiments were prepared using deionized water.

2.2 Materials synthesis

Firstly, aqueous solutions containing 10 mL of 0.5 mol L^{-1} $Zn(NO_3)_2 \cdot 6H_2O$ and 10 mL of 4.0 mol L^{-1} KOH were prepared at room temperature, respectively. The aqueous solution of $Zn(NO_3)_2 \cdot 6H_2O$ was dropped into the KOH solution under continuous stirring. Then different amount of CA was added and stirred in a series of experiments. A piece of zinc foil (1 cm × 1.2 cm) was suspended in the mixed solution at room temperature for 16 h. The reaction products were washed in KOH aqueous solution and rinsed with absolute ethanol repeatedly and then dried at 70 °C for 4 h.

2.3 Materials characterizations

The phase purity of the products were examined on a Bruker Model D8 Advance X-ray powder diffractometer with Cu K_α irradiation ($\lambda = 1.5418$ Å). The morphology and microstructure of the products were determined by field emission scanning electron microscopy (FESEM, Hitachi-S5500), transmission electron microscopy (TEM, Tecnai G^2 20, 200 kV), and high resolution TEM (HRTEM, JEM-2011, 200 kV). The Brunauer–Emmett–Teller (BET) surface area of the powders was analyzed by nitrogen adsorption–desorption isotherm curve measured at 77 K in a MicromeriticsASAP 2010 system. The sample was degassed at 180 °C before nitrogen adsorption measurements. The BET surface area was determined by a multipoint BET method. Photoluminescence (PL) measurement was conducted at room temperature using the 325 nm line of the He–Cd laser which was used as the excitation source. PL spectra were recorded by using a Hitachi luminescence spectrometer (F-4500).

2.4 Photocatalytic measurements

The photocatalytic activity was investigated using an organic dye *N*,*N*,*N*′,*N*′-tetraethylated rhodamine B (RhB) aqueous solution as a probe and a Pyrex beaker (250 mL) as the photoreactor vessel. The reaction suspension was prepared by adding 20 mg of samples into 100 mL of RhB solution with an initial concentration of 1.0×10^{-5} M. The aqueous solution was magnetically stirred in the dark for 1 h to reach a complete adsorption–desorption equilibrium. The suspension was then exposed to UV irradiation at room temperature. After initiation of the reaction by irradiation, a 5 mL sample of the suspension was taken out at regular intervals (~20 min) and centrifuged to completely remove the catalyst. In order to measure the RhB degradation, UV-visible spectra of the centrifuged solution was recorded by using UV-2550 UV-visible spectrophotometer (Shimadzu, Japan).

3. Results and discussion

The crystal structures of the as prepared products are characterized by using XRD technique. Fig. 1 shows typical XRD patterns of the samples synthesized in the mixed solution containing 10 mL of 0.5 mol L^{-1} $Zn(NO_3)_2 \cdot 6H_2O$ and 10 mL of 4.0 mol L^{-1} KOH with different amount of CA (0.1 g, 0.05 g, and 0 g). It can be seen that except for Zn peaks (marked with gray arrows), which come from the substrate, all the residual main peaks are well matched with the hexagonal ZnO according to the standard diffraction card (JCPDS number: 36-1451), indicating the formation of ZnO. It is also found that the relative

ratio of the (002) peak intensity to that of the (100) peak of ZnO (I_{002}/I_{100}) changes with the amount of CA. When the CA amount is 0.1 g, the value of I_{002}/I_{100} is 43, which is smaller than that of the standard pattern (77%), implying the preferential orientation of the sample is along the [100] direction. When the CA amount is decreased to 0.05 g, I_{002}/I_{100} increased to 75. Without the addition of CA, I_{002}/I_{100} value is *ca.* 138%, indicating a preferential growth along the [001] direction. The results will be further confirmed by HRTEM characterizations as discussed below.

Fig. 2 illustrates FESEM images of ZnO products obtained at room temperature for 16 h by using different CA amounts. The sample yielded with 0.1 g CA consists of flower-like microspheres with uniform size and shape as shown in Fig. 2a. The magnified SEM image (Fig. 2a inset) reveals that the microflowers are composed of 2D nanosheets with flat and smooth surface, and the thickness of the sheet is ~30–500 nm, while the other two dimensions reach micrometers. By carefully checking the high-magnification image of the microflowers, we find the edges of the assembled sheets show sawtooth-like morphology character (see the white arrows shown in Fig. 2b), hinting the occurrence of etching events. By decreasing the amount of CA to 0.05 g, ZnO flower-like microspheres with uniform size and shape are obtained (Fig. 2c). Fig. 2d is a high resolution SEM image of ZnO flower microspheres composed of 2D nanosheets as well as 1D nanoneedles. We notice that some nanoneedles align in the front of some nanosheets. It is therefore inferred that the nanoneedles are formed through the etching of the nanosheets. The obtained needle-sheet nanoflowers sample is named as ZnO N-SFs hereafter. Without the addition of CA, ZnO microspheres with homogeneous size and shape are obtained as can be seen in Fig. 2e. It is found that the ZnO flower-like 3DHNs are constituted by 1D nanoneedles with an average diameter of the tip and root about 30 and 120–150 nm, respectively, which is in agreement with previous studies (Fig. 2f, named as NFs hereafter).[21,22] In the following text, ZnO N-SFs (Fig. 2c and d) and NFs (Fig. 2e and f) are taken as typical examples to study the microstructures by employing TEM, HRTEM, and selected-area electron diffraction (SAED) methods.

Typical bright-field TEM images of the ZnO N-SFs are shown in Fig. 3a and b, which confirms that the constituted building blocks of ZnO 3DHNs are 2D nanosheets and 1D nanoneedles (see blue arrows in Fig. 3b). It also seems that the nanoneedles are formed by etching the nanosheets along one given direction since the needles are arranged in parallel. SAED pattern confirms that the N-SFs are single crystalline (Fig. 3b inset). A typical HRTEM image of a single nanoneedle on the tip of the nanosheet shows obvious 2D lattice fringes with spacing of ~2.56 and 2.80 Å, corresponding to the (002) and (100) planes of wurtzite ZnO, respectively (Fig. 3c), and the growth direction of nanoneedles is along [001]. By selecting different areas of the aligned nanoneedles, we find that all the nanoneedles possess single crystal structure nature and keep [001] as the growth direction (Fig. 3d and e).

Fig. 4a–c display TEM images of ZnO NFs and demonstrate the needle like morphology characteristics. The SAED pattern (Fig. 4c inset) indicates that the ZnO nanoneedle is single crystalline with [001] as growth direction. A typical HRTEM image of the tip of the needle marked with the white box in Fig. 4c shows 2D lattice fringes with spacing of ~2.63 and 2.84 Å, which correspond to the (002) and (100) planes of ZnO, respectively (Fig. 4d). Additional HRTEM images and

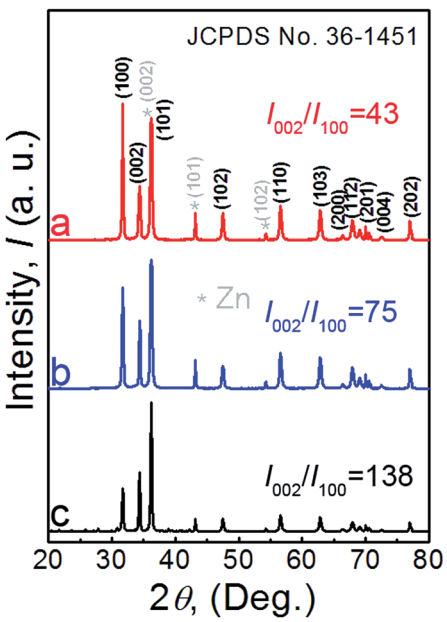

Fig. 1 XRD patterns of the products synthesized in the mixed solution containing 10 mL of 0.5 mol L^{-1} zinc $Zn(NO_3)_2 \cdot 6H_2O$, 10 mL of 4.0 mol L^{-1} KOH and different amount of citric acid. (a) 0.1 g, (b) 0.05 g, (c) 0 g.

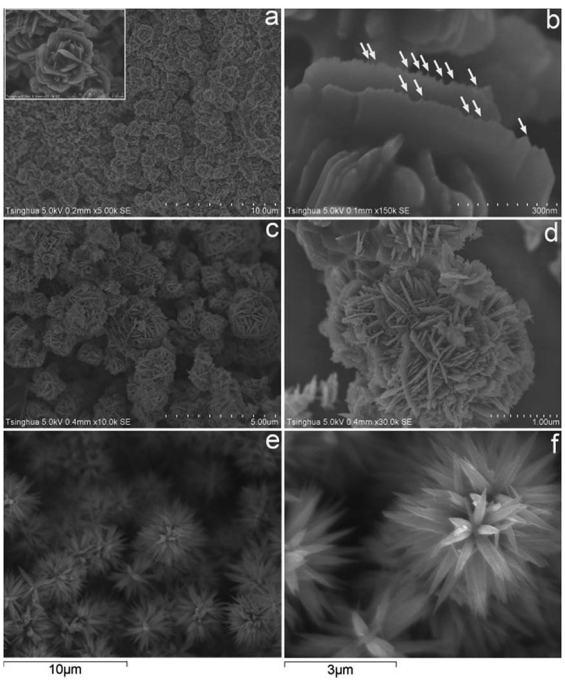

Fig. 2 FESEM images of the ZnO nanostructures with the addition of different amount of CA. (a and b) 0.1 g, (c and d) 0.05 g, (e and f) 0 g. The white arrows in (b) show the ZnO tips.

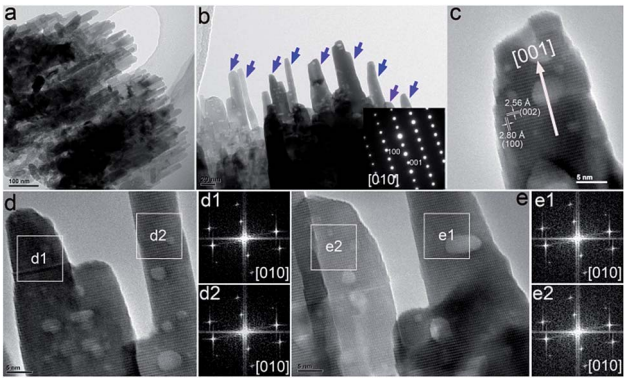

Fig. 3 (a and b) TEM and (c–e) HRTEM images of ZnO N-SFs, (d1–e2) FFT images corresponding to the marked rectangular areas, and the inset in (b) is the corresponding SEAD pattern. The blue arrows in (b) show the ZnO needles.

corresponding FFT patterns for other single nanostructure show that the nanoneedles are single crystalline with [001] as the growth direction (Fig. 4e–g).

A series of control experiments were performed to study the formation mechanism of ZnO 3DHNs. Fig. S1 (ESI†) displays the FESEM images of ZnO nanostructures with different amount of CA. Without the addition of CA, the sample exhibits NFs assembled by 1D nanoneedles (Fig. S1a†). As the CA amount increased to 0.05 g, ZnO N-SFs composed of nanosheets and nanoneedles are achieved (Fig. S1b†). When the amount of the added CA increased to 0.1 g, ZnO microflowers with 2D nanosheets as the building blocks are obtained, and the edges of the sheets have been etched (Fig. S1c†). Increasing CA amount to 0.5 g and 1.0 g, the yielded ZnO possess sheet like morphology (Fig. S1d and e†). A possible morphology controlling mechanism is proposed based on the observations described above (Fig. 5). As the aqueous solution of $Zn(NO_3)_2 \cdot 6H_2O$ is dropped into KOH aqueous solution under continuous stirring. Zn^{2+} present in the aqueous solution of $Zn(NO_3)_2 \cdot 6H_2O$ initiates the nucleation. This burst nucleation leads to the aggregation of supersaturated ZnO nuclei as shown in Fig. 5b (I, II). The involved reactions can be described as follows[21]

$$Zn^{2+} + 2OH^- \leftrightarrow Zn(OH)_2 \quad (1)$$

$$Zn(OH)_2 + 2OH^- \leftrightarrow [Zn(OH)_4]^{2-} \quad (2)$$

$$[Zn(OH)_4]^{2-} \rightarrow ZnO + H_2O + 2OH^- \quad (3)$$

According to our previous studies,[21] when the concentration of KOH is 4.0 mol L^{-1} (with no CA added), ZnO needle-like flowers are formed due to the etching behavior of KOH along [001] direction (Fig. 5b1, eqn (4)).

$$ZnO + 2OH^- \rightarrow ZnO_2^{2-} + H_2O \quad (4)$$

With the addition of CA, coordination between the Zn^{2+} ions of the (001) surface and the bulky $C_6H_5O_7^{3-}$ occurs due to the strong charge interaction,[42] *i.e.*, CA molecular prefers to absorb on (001) plane and thus slows down the crystal growth along [001] orientation.[14,42–44] Accordingly, the etching of KOH along [001] direction will be blocked. When the added amount of CA is very low (0.05 g), the capping effect is weak, resulting in the formation of the ZnO 3DHNs with nanoneedles and some partially etched nanosheets (Fig. 2d, 3 and 5b2). Increasing the CA amount will make more CA molecular cover on the (001) plane, and the etchant strength decreased along the [001] direction remarkably, which formed microflowers assembled by nanosheets with sawtooth-like edge (Fig. 2b and Fig. 5b3). If the CA amount is very high, the capping effect overcomes etching function, and only nanosheets are obtained. It should be mentioned here that, the presence of CA in the present alkaline solution consumes KOH and neutralizes the reaction solution through reaction (5). Such reduction in KOH amount also reduces its etchant effect.[42]

$$C_6H_8O_7 + 3OH^- \rightarrow C_6H_5O_7^{3-} + 3H_2O \quad (5)$$

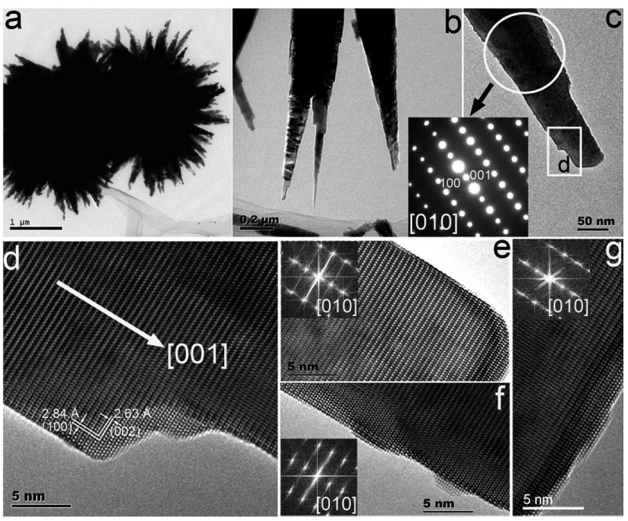

Fig. 4 (a–c) TEM and (d–g) HRTEM images of ZnO NFs, the insets in (e–g) show corresponding FFT images.

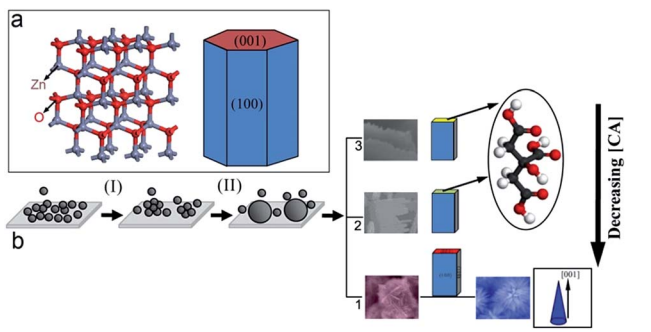

Fig. 5 Schematic illustration of the formation of ZnO nanostructures. (I) The initial burst nucleation occurs, (II) the aggregation of the supersaturated ZnO nuclei. The schematic in the frame show the ball and sticks model representation of the atoms arrangement and the illustration of typical crystal faces of wurtzite ZnO.

The nitrogen adsorption–desorption isotherms of ZnO N-SFs and NFs is shown in Fig. 6 to find the specific surface area. Both the isotherms reveal characteristics of mesoporous materials. The specific surface area of N-SFs and NFs calculated by BET equation is found to be 35.8 and 49.2 $m^2\ g^{-1}$, respectively. The corresponding pore size distribution curves (not shown here) show that the pores size falls in the size range from 2 to 30 nm. Mesoporous structure and high surface area of the obtained ZnO 3DHNs represents it as a good candidate for the diffusion and transportation of the degradable organic molecules and hydroxyl radicals in photochemical reaction, which will lead to effective photocatalytic performance.

The room temperature PL spectra of the ZnO N-SFs and NFs samples are illustrated in Fig. 7. Both spectra show a sharp ultraviolet (UV) emission centered at ~380 nm and a broad visible emission spanning from blue to red. The UV peak generally ascribes to the radiative annihilation of excitons or near-band-edge (NBE) transition. The visible emission is mainly originating from some self-activated centers, such as the singly ionized charge state of specific defects, and oxygen vacancies.[48,49] The relative intensity of UV emission increases from N-SFs to NFs, indicating the optical quality of NFs is better than that of N-SFs. Furthermore, the visible emissions is obviously blue shifted from ~560 nm for N-SFs to ~520 nm for NFs, which may due to the difference in morphology and the density of instinctive defects in the structures. Such defects-induced visible emissions shifts have also been reported previously.[21,50,51]

To analyze the photocatalytic activity of ZnO 3DHNs with different morphologies, ZnO N-SFs and NFs are taken as typical examples to photodegrade organic dye RhB under UV-irradiation. Fig. 8a and b shows a series of UV-vis absorption spectra of the aqueous solution of RhB with a 20 mg of N-SFs and NFs as the photocatalyst exposed to UV light for different duration. The characteristic absorption of RhB centered at 550 nm decreases rapidly for both N-SFs and NFs samples with extending the exposure time. This clearly makes both samples promising candidates in the class of photocatalyst for the degradation of RhB under UV light. Fig. 8c displays the comparison of the photocatalytic activity of ZnO N-SFs, NFs, and commercial ZnO powders under the same experimental conditions. As it can be clearly seen, the blank experiment (gray curve) with the absence of photocatalyst shows almost no degradation of RhB in UV light. While with the addition of different catalysts, the degradation of RhB is observed and the

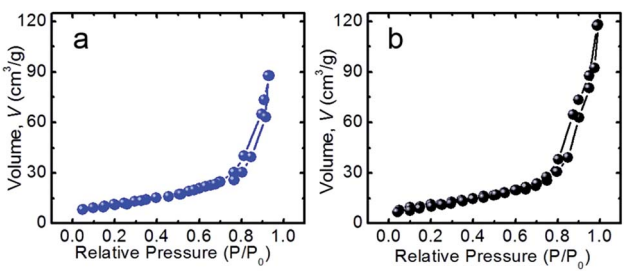

Fig. 6 Nitrogen adsorption–desorption isotherm of the ZnO (a) N-SFs and (b) NFs structures.

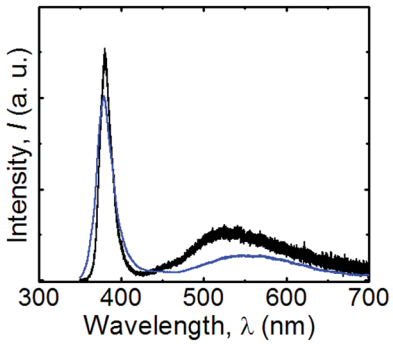

Fig. 7 Room temperature PL spectra from ZnO N-SFs (blue curve) and NFs (black curve).

photocatalytic activity depends on morphology of ZnO samples. The photocatalytic degradation of RhB follows the order: NFs > N-SFs > commercial ZnO powders. The linear relationship between $-\ln(C_t/C_0)$ and illumination time t (Fig. 8d) indicates that the photocatalytic degradation reaction follows pseudo-first-order kinetics, $-\ln(C_t/C_0) = kt$, where C_t is the concentration of the RhB, C_0 is the initial concentration of the RhB solution, and the slope k is the apparent reaction rate. The apparent photochemical degradation rate constant for the ZnO NFs is 0.016 min^{-1}, which is faster than that of ZnO N-SFs (0.011 min^{-1}) and ZnO powders (0.009 min^{-1}), which further confirms that the ZnO NFs are more effective in decomposing RhB in comparison with ZnO N-SFs and ZnO powders. In addition, degradation of RhB in aqueous solution under visible light irradiation ($\lambda > 420$ nm) also show that ZnO NFs exhibited excellent photocatalytic activities (Fig. S2, ESI†).

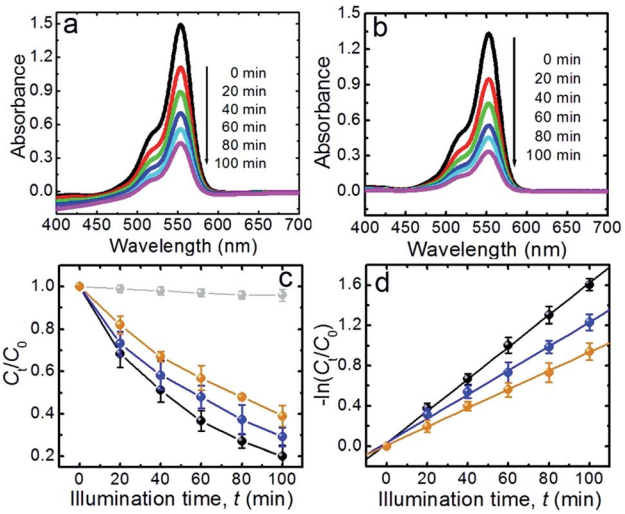

Fig. 8 Time dependent UV-vis spectral changes of RhB aqueous solution in the presence of (a) N-SFs and (b) NFs as the photocatalysts. (c) Photocatalytic degradation curves (C_t/C_0 *vs.* t) of RhB in the presence of different photocatalysts, including N-SFs (blue curve), NFs (black curve), commercial ZnO powders (orange curve), and without any photocatalyst (gray curve) under UV light exposure. (d) Linear fitting $-\ln(C_t/C_0)$ *vs.* t of the kinetic curves under UV light irradiation.

When the surfaces of ZnO nanostructures are illuminated by UV light with energy greater than the band gap energy, electron–hole pairs are generated as previously proposed in a mechanism for the degradation of organic dye.[52] The holes can react with water adhering to the surfaces of ZnO nanostructures to form highly reactive hydroxyl radicals (·OH). Those ·OH radicals have powerful oxidation ability in degrading organic dye.[53,54] It has been demonstrated that the higher PL intensity is favorable to produce ·OH radicals, and the above PL results show that the UV peak intensity of the NFs structure is higher as compared to N-SFs nanostructures. It is therefore the high optical quality of NFs that responsible for the enhanced photocatalytic activities. In addition, there are some other reasons for improving the photodegrade properties. (1) The exposed crystal facets. It is well known that catalytic properties are dependent on specific crystal facets, due to the unique dangling bond configurations.[1,2,55] Mclaren *et al.* reported that the polar (001) or (00−1) planes of ZnO have a stronger catalytic effect for the photocatalytic decomposition organic dye.[56] In our studies, CA molecular prefers to absorb onto (001) plane in ZnO N-SFs sample, resulting in less effective degradation of RhB as compared to ZnO NFs with clean (001) surface. (2) The active surface area and 3DHNs. The large active surface area and interspaces of the 3DHNs provides more chances for the diffusion and mass transportation of RhB molecules and the ·OH radicals in the photochemical reaction.

4. Conclusions

In summary, ZnO 3DHNs have been successfully synthesized by a simple and efficient wet chemical method at room temperature by using KOH and CA as etchant and capping agent, respectively. The morphology of the 3DHNs, including needle-sheet flowers and needle flowers, can be well controlled by changing the concentration of the reactant. A possible formation mechanism based on capping–etching competitive interactions has been proposed for the formation of distinct 3DHNs under different growth conditions. The room temperature PL properties of the products are also studied. The photocatalytic performance for the degradation of organic contaminants can be improved by fine tuning over the morphology of the 3DHNs. By careful selecting suitable capping agents and etchants, the present findings should be applicable to the synthesis and modification of other materials.

Acknowledgements

The authors would like to appreciate the financial supports from National 973 Project of China (2015CB654902) and Chinese National Natural Science Foundation (11374174, 51390471, 51401114). This work made use of the resources of the Beijing National Center for Electron Microscopy.

Notes and references

1 Y. Xia, Y. Xiong, B. Lim and S. E. Skrabalak, *Angew. Chem., Int. Ed.*, 2009, **48**, 60.
2 Z. Y. Zhou, N. Tian, J. T. Li, I. Broadwell and S. G. Sun, *Chem. Soc. Rev.*, 2011, **40**, 4167.
3 N. P. Dasgupta, J. Sun, C. Liu, S. Brittman, S. C. Andrews, J. Lim, H. Gao, R. Yan and P. Yang, *Adv. Mater.*, 2014, **26**, 2137.
4 H. L. Wang, J. Luo, A. Robertson, Y. Ito, W. J. Yan, V. Lang, M. Zaka, F. Schäffel, M. H. Rümmeli, G. A. D. Briggs and J. H. Warner, *ACS Nano*, 2010, **4**, 6659–6664.
5 J. Luo, J. Zhu, Z. P. Huang and L. Zhang, *Appl. Phys. Lett.*, 2007, **90**, 033114.
6 Y. H. Liu, W. Zhang, Y. J. Zhu, Y. T. Luo, Y. H. Xu, A. Brown, J. N. Culver, C. A. Lundgren, K. Xu, Y. Wang and C. S. Wang, *Nano Lett.*, 2013, **13**, 293.
7 H. B. Yao, H. Y. Fang, X. H. Wang and S. H. Yu, *Chem. Soc. Rev.*, 2011, **40**, 3764.
8 A. Kubacka, M. Fernández-García and G. Colón, *Chem. Rev.*, 2012, **112**, 1555.
9 B. Li and Y. Wang, *J. Phys. Chem. C*, 2010, **114**, 890.
10 H. C. Zeng, *J. Mater. Chem.*, 2011, **21**, 7511.
11 K. T. Nam, D. W. Kim, P. J. Yoo, C. Y. Chiang, N. Meethong, P. T. Hammond, Y. M. Chiang and A. M. Belcher, *Science*, 2006, **312**, 885.
12 H. Sun, M. Ahmad and J. Zhu, *Electrochim. Acta*, 2013, **89**, 199.
13 S. Yang, B. X. Yang, L. Wu, Y. H. Li, P. Liu, H. Zhao, Y. Y. Yu, X. Q. Gong and H. G. Yang, *Nat. Commun.*, 2014, **5**, 5355.
14 Z. R. Tian, J. A. Voigt, J. Liu, B. Mckenzie, M. J. Mcdermott, M. A. Rodriguez, H. Konishi and H. Xu, *Nat. Mater.*, 2003, **2**, 821.
15 H.-D. Yu, Z. Zhang and M.-Y. Han, *Small*, 2012, **8**, 2621.
16 Y. Wu, D. Wang, Z. Niu, P. Chen, G. Zhou and Y. Li, *Angew. Chem., Int. Ed.*, 2012, **51**, 1.
17 D. Wang, P. Zhao and Y. Li, *Sci. Rep.*, 2011, **1**, 37.
18 C. Chen, Y. Kang, Z. Huo, Z. Zhu, W. Huang, H. L. Xin, J. D. Snyder, D. Li, J. A. Herron, M. Mavrikakis, M. Chi, K. L. More, Y. Li, N. M. Markovic, G. A. Somorjai, P. Yang and V. R. Stamenkovic, *Science*, 2014, **343**, 1339.
19 M. J. Mulvihill, X. Y. Ling, J. Henzie and P. Yang, *J. Am. Chem. Soc.*, 2010, **132**, 268.
20 K.-Q. Peng, Y.-J. Yan, S.-P. Gao and J. Zhu, *Adv. Mater.*, 2002, **14**, 1164.
21 H. Y. Sun, Y. L. Yu, J. Luo, M. Ahmad and J. Zhu, *CrystEngComm*, 2012, **14**, 8626.
22 H. Y. Sun, Y. Chen, X. L. Wang, Y. W. Xie, W. Li and Y. X. Zhang, *J. Nanopart. Res.*, 2011, **13**, 97.
23 M. H. Huang, S. Mao, H. Feick, H. Q. Yan, Y. Y. Wu, H. Kind, E. Weber, R. Russo and P. D. Yang, *Science*, 2001, **292**, 5523.
24 S. Xu, Y. Qin, C. Xu, Y. G. Wei, R. S. Yang and Z. L. Wang, *Nat. Nanotechnol.*, 2010, **5**, 366.
25 F. Xu and L. T. Sun, *Energy Environ. Sci.*, 2011, **4**, 818.
26 Q. F. Zhang, C. S. Dandeneau, X. Y. Zhou and G. Z. Cao, *Adv. Mater.*, 2009, **21**, 4087.
27 E. S. Jang, J. H. Won, S. J. Hwang and J. H. Choy, *Adv. Mater.*, 2006, **18**, 3309.
28 B. Liu and H. C. Zeng, *J. Am. Chem. Soc.*, 2004, **126**, 16744.
29 X. Gao, X. Li and W. Yu, *J. Phys. Chem. B*, 2005, **109**, 1155.

30 J. Elias, C. Lévy-Clément, M. Bechelany, J. Michler, G.-Y. Wang, Z. Wang and L. Philippe, *Adv. Mater.*, 2010, **22**, 1607.
31 C. Lu, L. Qi, J. Yang, L. Tang, D. Zhang and J. Ma, *Chem. Commun.*, 2006, **33**, 3551.
32 X. Wu, H. Bai, C. Li, G. Lu and G. Shi, *Chem. Commun.*, 2006, 1655.
33 Y. Liu, J. Shi, Q. Peng and Y. Li, *J. Mater. Chem.*, 2012, **22**, 6539.
34 M. Huang, S. Weng, B. Wang, J. Hu, X. Fu and P. Liu, *J. Phys. Chem. C*, 2014, **118**, 25434.
35 S. Cho and K.-H. Lee, *Cryst. Growth Des.*, 2010, **10**, 1289.
36 L. Xu, Q. Chen and D. Xu, *J. Phys. Chem. C*, 2007, **111**, 11560.
37 C. V. Manzano, O. C. Calero, S. Hormeño, M. Penedo, M. Luna and M. S. M. González, *J. Phys. Chem. C*, 2013, **117**, 1502.
38 Y. Li, G. W. Meng and L. D. Zhang, *Appl. Phys. Lett.*, 2000, **76**, 2011.
39 F. Li, Y. Ding, P. Gao, X. Xin and Z. L. Wang, *Angew. Chem., Int. Ed.*, 2004, **43**, 5238.
40 Z. Zhang, H. Yuan, J. Zhou, D. Liu, S. Luo, Y. Miao, Y. Gao, J. Wang, L. Liu, L. Song, Y. Xiang, X. Zhao, W. Zhou and S. Xie, *J. Phys. Chem. B*, 2006, **110**, 8566.
41 J. Joo, B. Y. Chow, M. Prakash, E. S. Boyden and J. M. Jacobson, *Nat. Mater.*, 2011, **10**, 596.
42 S. Cho, J.-W. Jang, S.-H. Jung, B. R. Lee, E. Oh and K.-H. Lee, *Langmuir*, 2009, **25**, 3825.
43 L. Ge, X. Jing, J. Wang, J. Wang, S. Jamil, Q. Liu, F. Liua and M. Zhang, *J. Mater. Chem.*, 2011, **21**, 10750.
44 S. Das, K. Dutta and A. Pramanik, *CrystEngComm*, 2013, **15**, 6349.
45 X. Han, X. Zhou, Y. Jiang and Z. Xie, *J. Mater. Chem.*, 2012, **22**, 10924.
46 H. Wang, M. Li, L. Jia, L. Li, G. Wang, Y. Zhang and G. Li, *Nanoscale Res. Lett.*, 2010, **5**, 1102.
47 G.-W. She, X.-H. Zhang, W.-S. Shi, X. Fan, J. C. Chang, C.-S. Lee, S.-T. Lee and C.-H. Liu, *Appl. Phys. Lett.*, 2008, **92**, 053111.
48 H. Zheng, G. Duan, Y. Li, S. Yang, X. Xu and W. Cai, *Adv. Funct. Mater.*, 2010, **20**, 561.
49 L. W. Yin, Y. Bando, J. H. Zhan, M. S. Li and D. Golberg, *Adv. Mater.*, 2005, **17**, 1972.
50 G. Z. Shen, D. Chen and J. C. Lee, *J. Phys. Chem. B*, 2006, **110**, 15689.
51 M. Ahmad, X. X. Yan and J. Zhu, *J. Phys. Chem. C*, 2011, **115**, 1831.
52 H. C. Yatmaz, A. Akyo and M. Bayramoglu, *Ind. Eng. Chem. Res.*, 2004, **43**, 6035.
53 Q. J. Xiang, J. G. Yu, B. Cheng and H. C. Ong, *Chem.–Asian J.*, 2010, **5**, 1466.
54 H. B. Lu, H. Li, L. Liao, Y. Tian, M. Shuai, J. C. Li, M. Fhu, Q. Fu and B. P. Zhu, *Nanotechnology*, 2008, **19**, 045605.
55 N. Tian, Z. Y. Zhou, S. G. Sun, Y. Ding and Z. L. Wang, *Science*, 2007, **316**, 732.
56 A. Mclaren, T. V. Solis, G. Q. Li and S. C. Tsang, *J. Am. Chem. Soc.*, 2009, **131**, 12540.

